2014 IEEE International Conference on Robotics & Automation (ICRA)
Hong Kong Convention and Exhibition Center
May 31 - June 7, 2014. Hong Kong, China

Acoustic Flow for Robot Motion Control

Herbert Peremans[1] and Jan Steckel[1,2]

Abstract— **In this paper we explore the use of 3D acoustic flow fields to steer robot motion. We derive the 3D velocity fields set up by linear and rotational robot motions and explain how they can be sampled directly by a sonar array-sensor that we developed recently. The resulting acoustic flow field patterns are then shown to contain all the information necessary for controlling obstacle avoidance and corridor following behavior. Experimental data collected by the sonar system mounted on a wheelchair that was driven in an office environment are presented to validate the theoretically predicted acoustic flow patterns.**

I. Introduction

A large part of the robotics community has deemed in-air sonar sensing unable to support intelligent robot interactions with the world. We argue [1] that this conclusion is only warranted if one limits in-air sonar technology to the simple, widely available, range sensors [2]. Indeed, the wide variety of complex behaviors displayed by bats in total darkness proves that in-air sonar sensing does allow for rich interactions with complex environments [3]–[5]. Hence, for a sonar system to be useful for robot navigation in realistic environments, we have proposed [6] it should meet the following criteria: have a wide field of view (FOV), extract spatial information based on a single sonar reading and be able to cope with simultaneously arriving echoes. In [6] we describe a low-cost, yet powerful, in-air sonar system that combines broadband beamforming with a sparse, random array of receivers to meet these three criteria, i.e. it can produce 3D (=range, azimuth, elevation) location measurements for most reflecting objects within a large FOV (full hemisphere in front of the sonar system) in the presence of multiple overlapping echoes.

As shown by the many examples of flying insect's use of optical flow cues [7], [8], dynamic sensor cues contain a lot of information about both the spatial structure of an agent's environment as well as its ego-motion through that environment. In addition, the limited brain power available to insects as well as experiments with biomimetic robot models [9] indicate that these cues, when captured in a smart way, require minimal further processing to allow steering important basic navigation behaviors. While the use of acoustic flow cues for similar purposes in bats has been studied much less, both software simulation studies [10] as well as a few experimental studies with bats [11] have shown the suitability of such cues for guidance of bat sensorimotor routines. Hence, we propose that, as is the case for optic flow cues, acoustic flow cues both contain sufficient information as well as directly available information, i.e. requiring limited further processing, to guide basic navigation behaviors.

In the past, a number of attempts have been made to use acoustic flow cues for robot motion control. In [12] proof-of-concept robotic experiments are described that show that Doppler shift cues resulting from the use of long, constant frequency, calls contain sufficient information to implement rudimentary obstacle-avoidance and convoy navigation. The extraction of relative velocity to control robotic obstacle avoidance behavior is described in [13]. In this paper, standard optical flow techniques are applied to artificial images constructed from binarized occupancy grids based on the readings of ultrasonic range sensors. In [14] an optical flow approach is applied to the segmentation, 2-D motion estimation, and subsequent tracking of observations in sector scan sonar images. In [15] an acoustic flow theory is derived and preliminary results are presented for the case of a single monaural CTFM-sonar (Continuous Transmission, Frequency Modulation) sensor [16] and a single reflecting object. While the work described in [17] is not truly an application of acoustic flow, it groups sensor readings belonging to the same environmental features based on the ego-motion induced constraints, referred to as flow lines in the text below, consecutive sensor readings have to comply with. In this work it is also noted that a polar (2D) or spherical (3D) representation is more appropriate than a Cartesian representation for formulating these constraints in. Hence, we propose that the readings of the 3D in-air sonar system we developed are particularly well suited for sampling the acoustic flow field set up by ego-motion of a robotic agent.

The remainder of the paper is structured as follows: in section II we present a brief description of the array sensor used and the environmental representation it gives rise to. In section III we describe the equations that govern the acoustic flow field set up by particular robot motions as sampled by our in-air sonar system. Section IV contains experimental validation of the theoretically derived flow-field patterns. The main conclusions are stated in section V.

II. Array sensor

In this section we present a brief overview of the in-air sonar system used for the acoustic flow experiments. A more detailed description of this system can be found in [6].

A. Hardware Overview

The digital subsystem of the sonar sensor consists of an FPGA, memory, 32 12-bit ADC's (312-500 kS/sec) and is connected by USB interface to a PC. The receiver

[1]FTEW-ENM, University of Antwerp, 2000 Antwerp, Belgium herbert.peremans@uantwerpen.be
[2]Centrum Voor ZorgTechnologie, University of Antwerp, 2000 Antwerp, Belgium

subsystem contains 32 amplifiers and (Knowles FG-23329) microphones. Finally, the emitter subsystem contains a single 12-bit DAC (250kS/sec), a high voltage amplifier and a Polaroid transducer. For the emitted signal we chose a hyperbolic chirp, i.e. a sinusoidal signal with instantaneous frequency hyperbolically swept from a start frequency of 100kHz down to a stop frequency of 20kHz in 3msec. The amplitude of the call is modulated by a hamming window.

B. Signal Processing

The array consists of 32 microphones, each receiving their own copy of the echo signal, denoted by $s_i^M[k]$ with $i = 1...32$ and k, the discrete timesamples, ranging from 0 to K. The received signals are processed using a matched filter:

$$s_i^{MF}[k] = \mathcal{F}^{-1}\left\{ S_i^M(j\omega) \cdot S_b^*(j\omega) \right\} \tag{1}$$

with $\mathcal{F}^{-1}$ denoting the inverse Discrete Fourier Transform (DFT), $S_i^M(j\omega)$ the Discrete Fourier transform of the i-th microphone signal $s_i^M[k]$ and $S_b^*(j\omega)$ the complex conjugate of the Discrete Fourier transform of the emitted signal, as approximated by the signal sent to the DAC. After the matched filter operation, the beamforming process takes place. We use direction vector ψ to refer to reflector positions in the far-field of the sensor. The Delay-and-Sum beamforming process can then be written as

$$s_\psi^{BF}[k] = \sum_{i=1}^{32} w_i \cdot s_i^{MF}\Big[k + \tau_i(\psi)\Big], \tag{2}$$

with w_i the weight (a real scaling factor) for the i-th microphone, $\tau_i(\psi)$ the delay, relative to the chosen reference channel of the array, for the i-th microphone for direction ψ, and s_i^{MF} the output of the matched filter in the i-th microphone channel After beamforming, the envelope $s_\psi^{EN}[k]$ of the signal $s_\psi^{BF}[k]$ is extracted as the representation of the reflector distribution in direction ψ, with the time axis coding for the ranges of the reflectors in that direction.

C. Energy scape representation

We introduced the energy scape (ES) in [6] as representation of the 2D or 3D spatial distribution of reflectors by means of the amount of energy the reflectors reflect back to the sensor at each distance and from each direction of interest. For a set of directions ψ, e.g. defined by spherical coordinates, the ES is formed by combining the envelopes $s_\psi^{EN}[k]$ in the structure

$$E(k,\psi) = \begin{bmatrix} s^{EN}_{(\varphi_1,\vartheta_1)}[k] & s^{EN}_{(\varphi_2,\vartheta_1)}[k] & \dots & s^{EN}_{(\varphi_n,\vartheta_1)}[k] \\ s^{EN}_{(\varphi_1,\vartheta_2)}[k] & s^{EN}_{(\varphi_2,\vartheta_2)}[k] & \dots & s^{EN}_{(\varphi_n,\vartheta_2)}[k] \\ \dots & \dots & \dots & \dots \\ s^{EN}_{(\varphi_1,\vartheta_m)}[k] & s^{EN}_{(\varphi_2,\vartheta_m)}[k] & \dots & s^{EN}_{(\varphi_n,\vartheta_m)}[k] \end{bmatrix}$$

with m the number of sampled azimuth directions and n the number of sampled elevation directions. By choosing the sampling of the frontal hemisphere in accordance with task requirements processing resources can be economized, as the beamforming effort is directly proportional with the number of directions. For example, if one varies the azimuth angle $\varphi = -90°...90°$ and keeps the elevation angle constant ($\vartheta = 0°$), one gets the 2D ES representing the reflected energy distribution in the horizontal plane

$$E(k,\varphi) = \begin{bmatrix} s^{EN}_{\varphi_1}[k] & s^{EN}_{\varphi_2}[k] & \dots & s^{EN}_{\varphi_n}[k] \end{bmatrix}$$

with n the number of azimuth directions φ. In summary, the environmental sampling strategy used to build the ES can be optimized for the task at hand to provide the maximum amount of information with the minimum computational effort.

III. Acoustic flow field

In this section we derive the acoustic flow fields arising from the execution of particular robot motions.

A. General 3D velocity field

For the derivation of the 3D velocity field defined by a particular robot ego-motion we assume stationary reflectors in general 3D positions. We use a 'conical coordinate'-system (see Fig.1) to denote the position of a reflector in the robot body reference frame by the vector (r, θ, φ) with $\theta \in [0, \pi/2]$ for the frontal hemisphere of the robot and $\varphi \in [0, 2\pi]$. This coordinate system is related to the standard cartesian coordinates by

$$\overrightarrow{x}(t) = \begin{bmatrix} x(t) \\ y(t) \\ z(t) \end{bmatrix} = \begin{bmatrix} r(t)\cos\theta(t) \\ -r(t)\sin\theta(t)\sin\varphi(t) \\ r(t)\sin\theta(t)\cos\varphi(t) \end{bmatrix}. \tag{3}$$

The time derivatives of the coordinates, expressed in the

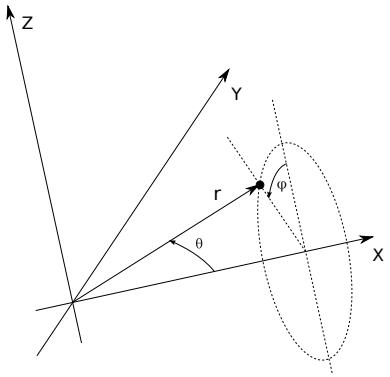

Fig. 1. The conical coordinate system (r, θ, φ).

moving robot body reference frame, of a stationary reflector are given by

$$\frac{d\overrightarrow{x}}{dt} = -\overrightarrow{v}_{rob} - \overrightarrow{\omega}_{rob} \times \overrightarrow{x}, \tag{4}$$

with $\overrightarrow{v}_{rob}$ the linear velocity vector and $\overrightarrow{\omega}_{rob}$ the rotational velocity vector of the robot, expressed in the robot body reference frame, and $\times$ denoting the cross product.

If we choose the x-axis of the robot body reference frame to coincide with the direction of the linear velocity vector

and limit the robot to planar movement, i.e. rotations about its z-axis only, the velocity vectors are given by

$$\overrightarrow{v}_{rob} = \begin{bmatrix} V \\ 0 \\ 0 \end{bmatrix}, \quad \overrightarrow{\omega}_{rob} = \begin{bmatrix} 0 \\ 0 \\ \omega \end{bmatrix}, \tag{5}$$

with V and ω the magnitudes of the linear and angular velocities respectively. We will assume these magnitudes to be constant for the duration of a single sonar measurement. Taking the derivative of Eq. (3)

$$\frac{d\overrightarrow{x}}{dt} = \begin{bmatrix} c\theta & -rs\theta & 0 \\ -s\theta s\varphi & -rc\theta s\varphi & -rs\theta c\varphi \\ s\theta c\varphi & rc\theta c\varphi & -rs\theta s\varphi \end{bmatrix} \cdot \begin{bmatrix} dr/dt \\ d\theta/dt \\ d\varphi/dt \end{bmatrix} \tag{6}$$

with $r, c\theta, s\theta, c\varphi, s\varphi$ denoting $r(t), \cos\theta(t), \sin\theta(t), \cos\varphi(t), \sin\varphi(t)$ respectively. Substituting this result and Eqs. (3) and (5) in Eq. (4) we can express the 3D velocity field due to robot ego-motion as

$$\begin{bmatrix} dr/dt \\ d\theta/dt \\ d\varphi/dt \end{bmatrix} = \begin{bmatrix} -\cos\theta(t) & 0 \\ \sin\theta(t)/r(t) & \sin\varphi(t) \\ 0 & \tan\theta(t)\cos\varphi(t) \end{bmatrix} \cdot \begin{bmatrix} V \\ \omega \end{bmatrix} \tag{7}$$

in each point (r, θ, φ).

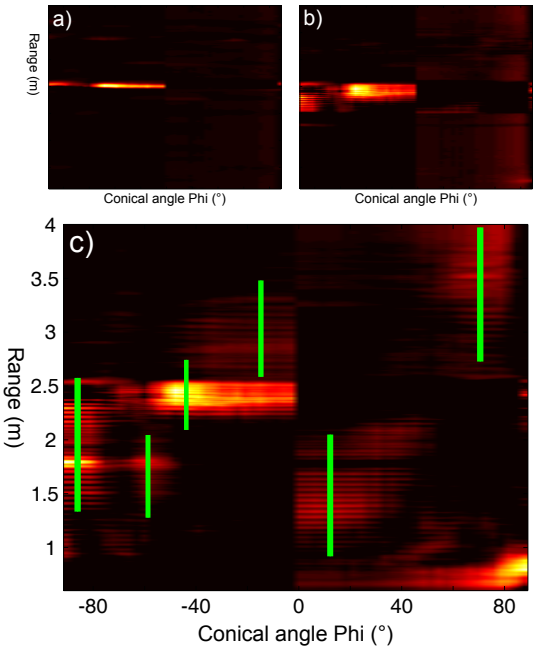

Fig. 2. r-φ representation of the sonar data. Accumulated data over a linear trajectory results in constant-φ trajectories, illustrating the $\varphi(t) = C_\varphi$ constraint.

B. Linear movement

In the case of a linear robot movement, i.e. $\omega = 0°$/sec, we conclude from Eq. (7) that $d\varphi/dt = 0$. Hence, $\varphi(t) = C_\varphi$ is an invariant of this type of movement. To illustrate this invariant, we have mounted the 3D sonar system on a wheelchair and drove along a linear trajectory in an office hallway. The wheelchair was aligned with the direction of the hallway and closer to the left side of the hallway. Data was captured, and the ES were calculated in the conical coordinate system. Consecutive measurements where accumulated in a memory E_t^C by using a maximum operator: as a new measurement is taken, each voxel in the accumulated energy scape is updated, and gets assigned the maximum of the old value of that voxel and the current ES

$$E_{t+1}^C = max(E_t^C, E_t) \tag{8}$$

In a next step, the θ-dimension is integrated out, yielding a 2D (φ, r) structure containing information on the complete trajectory. This structure is shown in Fig. 2 c). Targets present in the data should appear in the image as vertical (= constant ϕ) trajectories. Some of these trajectories have been marked by green lines. Insets a) and b) show intermediate results of the accumulated 2D structure.

For the other two coordinates $(r(t), \theta(t))$, Eq. (7) now reduces to

$$\begin{aligned} dr/dt &= -V \cdot \cos(\theta(t)) \\ d\theta/dt &= \frac{V \cdot \sin(\theta(t))}{r(t)}. \end{aligned} \tag{9}$$

The solution to this set of differential equations has to comply with

$$\frac{\dot{r}(t)}{r(t)} = -\frac{\dot{\theta}(t)}{\tan(\theta(t))}$$

for $\theta_0 \neq 0$ with θ_0 defined as the angle between the robot path and the line of sight to a particular reflector at its first sighting. Equivalently,

$$r(t) \cdot \sin(\theta(t)) = C$$

for $\theta_0 \neq 0$ with C a constant. This expression describes the second invariant for linear robot motions defining the different flow lines, i.e. the solutions of the differential equations Eq. (9) for different initial conditions (r_0, θ_0). As can be seen from Fig. 3(a) this motion invariant can also be interpreted as the orthogonal distance from a reflector to the linear path of the robot making it obvious that it should stay constant. In case $\theta_0 = 0$ then $d\theta/dt = 0 \Leftrightarrow \theta(t) = 0$ and $dr/dt = -V \Leftrightarrow r(t) = r_0 - V \cdot t$. The full flow line pattern, i.e. the time-trajectories in (r, θ)-space associated with different initial reflector positions, $r \cdot \sin(\theta) = r_0 \cdot \sin(\theta_0)$, are shown in Fig. 3(b). As time progresses and the robot moves along its linear path, the images in (r, θ)-space of the visible reflectors will trace these trajectories. Note that as the trajectories in (r, θ)-space are independent of $\varphi(t)$ and as $\varphi(t) = C_\varphi$, we have not shown this third coordinate.

C. Pure rotation movement

In the case of a pure rotation of the robot, i.e. $V = 0$m/sec, we conclude from Eq. (7) that $dr/dt = 0$. Hence, $r(t) = C_r$ is an invariant of this type of movement, as expected. For the other two coordinates $(\theta(t), \varphi(t))$, Eq. (7) now reduces

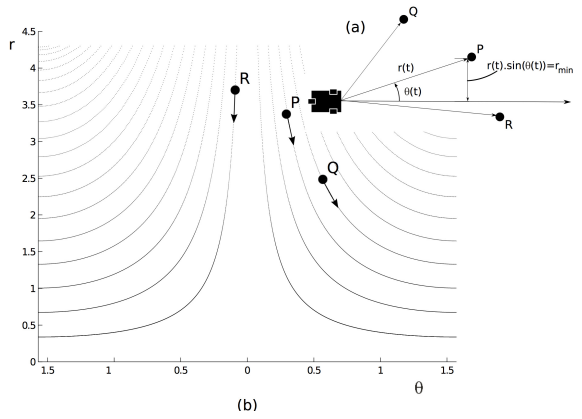

Fig. 3. (a) Motion invariant associated with reflector P for linear robot path (top view); (b) the $(r(t), \theta(t))$ trajectories (=flow lines) corresponding with the reflectors R, P and Q. We show reflector distances falling in the range of interest ($r \in [0, r_{max}]$) with r_{max} the maximum range of the sonar sensor. We further limit ourselves to the region in front of the robot ($\theta \in [0, \pi/2]$), as defined by the direction of motion of the robot.

to

$$\begin{aligned} d\theta/dt &= \omega \cdot \sin(\varphi(t)) \\ d\varphi/dt &= \omega \cdot \tan(\theta(t)) \cos(\varphi(t)). \end{aligned} \quad (10)$$

In this case the flow lines in $(r(t), \theta(t))$-space will be horizontal lines, as illustrated in Fig. 4.

In the case of the robot following a curved path both a rotation and a translation of the robot will occur. In that case the final flow field will be a linear combination of the two flow fields described above, as can be deduced from Eq. (7).

It is important to realize that the 3D velocity fields set up by linear and/or rotational movements of the robot are sampled directly by our sonar sensor. This is different for optical sensors where the optical flow field is the projection of the 3D velocity field onto the 2D image surface. Hence, the trajectories described above are also the flow lines of the acoustic flow field set up by the robot's movement.

IV. Experimentally validated acoustic flow fields for particular robot navigation behaviors

We now focus on how the acoustic flow patterns that occur in the course of specific robot motions can be used to generate navigation behavior primitives. To illustrate the occurring acoustic flow patterns in their simplest manifestation we have made use of an experimental platform (=wheelchair) that moves in the horizontal plane only. Furthermore, we have programmed the sonar to restrict its sampling of the 3D vector field to the horizontal plane as well. In terms of the conical coordinate system defined above, the section of the horizontal plane sampled by the sensor is described by $r \in [0, r_{max}]$, $\theta \in [0, \pi/2]$ and $\varphi = 3\pi/2$ for the left (relative to the motion direction) half plane and $\varphi = \pi/2$ for the right half plane.

A. Obstacle avoidance

The motion invariant $r(t) \cdot \sin(\theta(t)) = C$ can be used to define a simple obstacle avoidance algorithm. To this end we introduce r_{safe} to denote the minimal obstacle distance from the center of the robot for safe passage. Any reflector whose trajectory falls within the collision zone in $(r(t), \theta(t))$-space is on a collision course with the robot, see Fig. 4. This collision zone consists of two subregions: (i) a bearing-independent band for all distances closer than r_{safe} and (ii) a bearing-dependent band containing all trajectories that correspond with obstacles at distance $r_{min} \cdot \sin(\pi/2) < r_{safe}$, with r_{min} the orthogonal distance between the obstacle and the wheelchair's path.

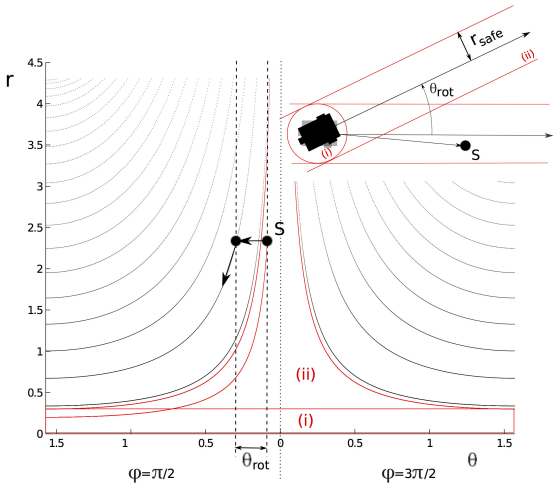

Fig. 4. By rotating the robot can avoid collisions with reflectors whose images fall within the collision zone in $(r(t), \theta(t))$-space.

The obstacle avoidance algorithm should ensure that reflector trajectories that fall in subregion (ii) are moved out of it before the reflector trajectory enters subregion (i). This can be effected by rotating the robot. From Eq. (10) we see that for such robot motion $d\varphi/dt = 0$ for $\varphi = 3\pi/2$ and $\varphi = \pi/2$, mapping object images in the horizontal plane onto that same plane again. We also note that $d\theta/dt = \pm\omega$ for $\varphi = \pi/2$ and $\varphi = 3\pi/2$ respectively. Hence, when the robot is rotated the direction of robot motion changes and all reflector images in (r, θ)-space are shifted horizontally by $|\theta_{rot}|$ for a robot rotation angle of θ_{rot} (see Fig. 4). Hence, the task of the obstacle avoidance algorithm is to shift the reflector trajectories that fall within the collision zone out of it by rotating the robot over the appropriate amount. Note that we assume that the robot rotates on the spot before continuing its linear path.

Whenever a reflector trajectory would enter the subregion (i) of the collision zone the robot should be stopped, backed up and rotated on the spot until the collision zone is reflector free again. If this is impossible, it means the robot is completely surrounded by reflectors and no exit path is available.

Fig. 5 shows the acoustic flow in the ES during an obstacle avoidance task. The green flowlines in the ES indicate the collision zone: objects present in this area will lead to collisions with the wheelchair if a linear trajectory is followed. Once the wheelchair detects objects in the collision

zone (subplot a), it performs a rotation (subsets b-c) until the object is shifted out of the collision zone, and resumes its linear trajectory (subset d).

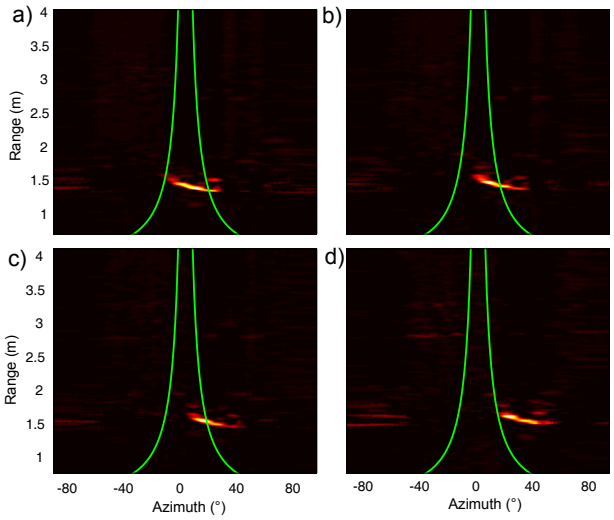

Fig. 5. Experimental results showing the acoustic flow during obstacle avoidance. The green flowlines indicate the collision zone for the current wheelchair position. The images show the evolution of the ES as the wheelchair performs a pure rotation.

B. Corridor following

A corridor following algorithm can also be derived from the reflector representation in (r, θ)-space. Assuming the robot movement is aligned with the centerline of the corridor, the images of the reflectors in $(r(t), \theta(t))$-space will fall on two symmetric trajectories as shown in Fig. 7(a). Deviations from movement along the centerline will result in deviations from this symmetric acoustic flow pattern. If the robot movement is aligned with the corridor but off-center, the acoustic flow pattern will still consist of two trajectories only but they will now be asymmetric (see Fig. 7(b)). To move towards the centerline of the corridor again, the robot should move away from the side that contains the trajectory with the lowest r_{min}. For non-aligned movement in the corridor the acoustic flow patterns will no longer consist of two trajectories, instead asymmetric patterns such as the one shown in Fig. 7(c) will result.

Fig. 6 shows experimental results of the wheelchair following a linear trajectory in an office hallway. The wheelchair moves off-center (closest to the left wall), mostly following the direction of the hallway. Subplots a)-c) show the ES for different times along the linear trajectory. The green flowline corresponds to the reflecting features of the left wall. As can be seen, the object images fall on the flowline as the wheelchair executes the linear trajectory. Subset d) shows the integration of the ES activity over all different possible flowlines, and integrated over the linear trajectory. As expected, the integrated data peaks at the position ($= r_{min}$) of the flowline corresponding to the left wall.

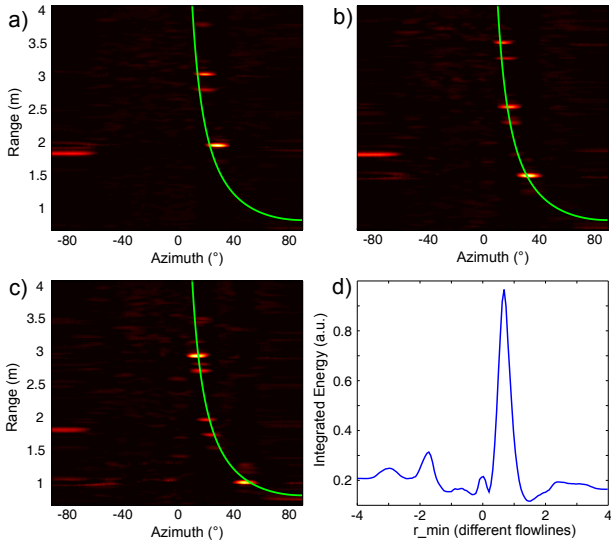

Fig. 6. Experimental Results showing the acoustic flow in the case of (off-center) corridor following by the wheelchair. Subplots a-c) show the ES for different times along the linear trajectory. Subset d) shows the integration of the ES activity over different flow lines, averaged over the linear trajectory.

V. Conclusions and Future Work

In this work we have presented a mathematical framework which allows to extract environmental information from acoustic flow using a 3D sonar sensor. We show how this information can be used to control basic navigation behaviors like obstacle avoidance and corridor following. As the 3D sonar sensor directly samples the 3D velocity field in the proposed spherical-conical coordinate system, the necessary information needed to drive our models is readily available. Using robotic experiments in realistic indoor environments we have shown that the proposed models hold and that navigation primitives can be constructed based on acoustic flow. Future work will attempt the closure of the control loop: performing real-time feedback of acoustic flow cues to steer the robot's motion. Furthermore, the integration of data over flow lines will be made adaptive to the actual motions performed by the robot. This will allow us to eliminate noise from the acoustic flow data, enhancing the robustness of the proposed scheme.

Acknowledgments

This work was funded by a grant from the Promobilia Foundation, and the authors gratefully acknowledge the support of the Industrial Research Fund of the University of Antwerp

References

[1] H. Peremans, F. de Mey, and F. Schillebeeckx, *Frontiers in sensing : from biology to engineering*. Springer Berlin, 2012, ch. Man-made versus biological in-air sonar systems.

[2] C. Biber, S. Ellin, E. Shenk, and J. Stempeck, "The polaroid ultrasonic ranging system," *67th Convention of the Audio Engineering Society*, October 1980.

[3] N. Ulanovsky and C. Moss, "What the bat's voice tells the bat's brain," *Proceedings of the National Academy of Sciences*, vol. 105, no. 25, p. 8491, 2008.

[4] H. Schnitzler, C. Moss, and A. Denzinger, "From spatial orientation to food acquisition in echolocating bats," *Trends in Ecology & Evolution*, vol. 18, no. 8, pp. 386–394, 2003.

[5] D. Griffin, "Listening in the dark: the acoustic orientation of bats and men." 1958.

[6] J. Steckel, A. Boen, and H. Peremans, "Broadband 3-d sonar system using a sparse array for indoor navigation," *Robotics, IEEE Transactions on*, vol. 29, no. 1, pp. 161–171, 2013.

[7] M. V. Srinivasan, "Visual control of navigation in insects and its relevance for robotics," *Current Opinion in Neurobiology*, vol. 21, no. 4, pp. 535–543, 2011.

[8] N. Franceschini, F. Ruffier, and J. Serres, "A bio-inspired flying robot sheds light on insect piloting abilities," *Current Biology*, vol. 17, no. 4, pp. 329 – 335, 2007. [Online]. Available: http://www.sciencedirect.com/science/article/pii/S0960982206026662

[9] J. S. Humbert and A. M. Hyslop, "Bioinspired visuomotor convergence," *Robotics, IEEE Transactions on*, vol. 26, no. 1, pp. 121–130, 2010.

[10] R. Muller and H. Schnitzler, "Acoustic flow perception in cf-bats: Properties of the available cues," *The Journal of the Acoustical Society of America*, vol. 105, p. 2958, 1999.

[11] D. Lee, F. Weel, T. Hitchcock, E. Matejowsky, and J. Pettigrew, "Common principle of guidance by echolocation and vision," *Journal of Comparative Physiology A: Neuroethology, Sensory, Neural, and Behavioral Physiology*, vol. 171, no. 5, pp. 563–571, 1992.

[12] J. M. Carmena and J. C. Hallam, "The use of doppler in sonar-based mobile robot navigation: inspirations from biology," *Information Sciences*, vol. 161, no. 1, pp. 71–94, 2004.

[13] C. Park and C. Lee, "Sonar sensor data processing based on optical flow in robot navigation," *Proceedings of the Institution of Mechanical Engineers, Part I: Journal of Systems and Control Engineering*, vol. 225, no. 1, pp. 1–7, 2011.

[14] D. M. Lane, M. J. Chantler, and D. Dai, "Robust tracking of multiple objects in sector-scan sonar image sequences using optical flow motion estimation," *Oceanic Engineering, IEEE Journal of*, vol. 23, no. 1, pp. 31–46, 1998.

[15] P. McKerrow, "Acoustic flow," in *IEEE/RSJ International Conference on intelligent Robots and Systems, IROS*. IEEE, 2008, pp. 1365–1370.

[16] L. Kay, "A sonar aid to enhance spatial perception of the blind: Engineering design and evaluation," *Radio and Electronic Engineer*, vol. 44, no. 11, pp. 605–627, 1974.

[17] R. Rikoski and J. Leonard, "Trajectory sonar perception," in *Robotics and Automation, 2003. Proceedings. ICRA'03. IEEE International Conference on*, vol. 1. IEEE, 2003, pp. 963–970.

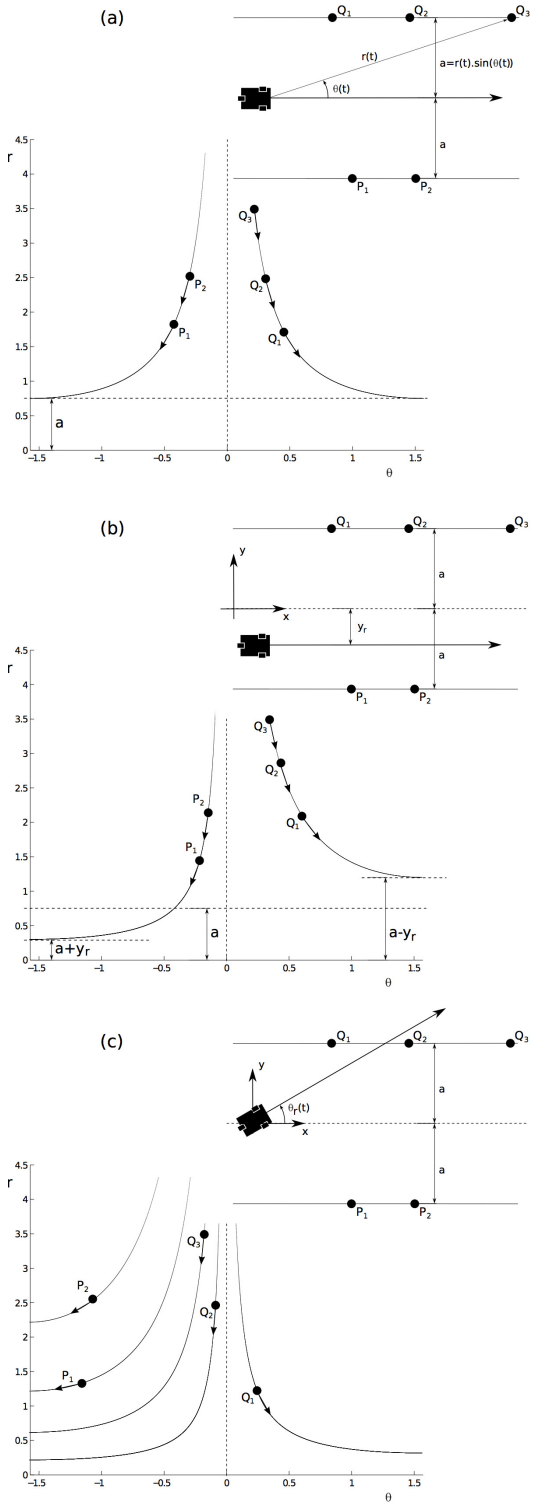

Fig. 7. Acoustic flow patterns caused by specific movements in a corridor. (a) Movement along the centerline of the corridor. The specific trajectories are determined by the width $2a$ of the corridor. (b) Off-center movement along the corridor. The specific trajectories are determined by both the width $2a$ of the corridor and the off-center distance y_r. (c) Movement not aligned with the corridor.